

Stick-slip dynamics in an interleaved system with self-amplified friction

A. Plati,¹ F. Restagno,¹ and C. Pouillard¹

¹Université Paris-Saclay, CNRS, Laboratoire de Physique des Solides, 91405 Orsay, France

Understanding how stick-slip dynamics manifests in diverse physical conditions is a crucial topic in tribology. Although it has been extensively studied in simple frictional configurations, the characterization of stick-slip behavior in complex assemblies is challenging. This work presents the first systematic investigation of stick-slip dynamics in a system with multiple contact surfaces undergoing friction amplification through conversion of traction forces into normal compression. Using interleaved paper blocks as a model system, we combine force measurements and image processing to characterize stick-slip events occurring when the two blocks are pulled apart at different detachment velocities. We find that both the peak force and the amplitude of the stick-slip events decrease along with the system's detachment. By combining a previously designed model for friction amplification and the stick-slip dynamics predicted by a simple frictional spring-block system, we link the observed behavior to the evolving normal compression within the assembly. Through force measurements and imaging, we extract the effective stiffness of the system from stick-slip events at low velocities and relate it to the system's normal compression. We then predict the observed decrease of the global stiffness as function of the detachment by considering the spatial distribution of normal forces within the assembly, which determines an effective number of sheets contributing to the system's mechanical response. Our findings reveal a non-trivial interplay between internal stress distribution and mechanical response mediated by frictional forces, with implications for granular materials, textiles, fibrous systems, and mechanical metamaterials.

I. INTRODUCTION

Friction [1, 2] is present in countless aspects of daily life, allowing us to walk and experience sensory perception [3]. In addition to these useful properties, friction dissipates mechanical energy as heat through potentially destructive mechanisms such as wear. This makes a fundamental understanding of friction a central topic in tribology, with important applications in industrial manufacturing processes. The simplest laws of friction were first formulated by Da Vinci [4] and then rediscovered and formalized by Amontons and Coulomb [5]. The modern framework of tribology was subsequently established by Bowden and Tabor [6]. A defining dynamical characteristic of friction is stick-slip motion [7]: when the coefficient of kinetic friction is lower than the static one, sliding surfaces undergo alternating cycles of adhesion and slipping with varying regularity. This nonlinear dynamics manifests across diverse phenomena in both soft and hard condensed matter systems, spanning scales from nanometric contacts to seismic faults [8–19]. Understanding how stick-slip motion manifests in diverse physical conditions (e.g., dry, wet, worn surfaces [20–22]) is then crucial for a wide range of disciplines, as is the idea of controlling its dynamical features [23, 24].

Standard laboratory and theoretical investigations of friction consider two surfaces in contact under applied tangential and normal forces [8, 10, 25–27]. The tangential force drives relative sliding, while the normal force, independent of the tangential one, enhances contact strength by increasing both static and dynamic friction. However, many real systems—particularly those involving granular, textile, and fibrous materials—consist of complex assemblies of deformable objects with many surfaces in contact at the same time. In these systems,

structural deformation can convert the traction force into orthogonal components, thereby amplifying the normal load and enhancing frictional resistance. This geometric conversion mechanism gives rise to distinct friction amplification phenomena. A first example is provided by the belt friction, which occurs when a deformable object such as a cable or a belt is wrapped around a rigid body like a rod, as seen in capstans used on ships. In these systems, the friction force is generated by the traction that is applied [28]. Recent research proposes that the capstan effect may also underlie the process by which DNA interacts with bacteriophage capsids [29]. Another illustrative case is the Chinese finger trap, which relies on a woven helical braid that tightens around the fingers as it is pulled. This braiding mechanism is relevant to surgical sutures [30] and potentially to the frictional behavior observed in F-actin filament bundles [31]. Multicontact assemblies further involve complex interplay between internal stress distribution, heterogeneities, and overall frictional or cohesive behavior. Indeed, different contact surfaces in static traction or relative motion within the assembly may experience variable amounts of normal compression, depending on their specific position. For example, we can consider the distribution of internal stresses in fibrous materials, such as ropes [32–34] or textiles [35–37], when they are subjected to tensile strain.

A crucial problem in these systems is relating individual microscopic contact properties to large-scale effects, such as the onset of shear thickening or avalanches in granular systems [38, 39]. It is also important to mention that the emergent mechanical behavior related to friction amplification in multicontact assemblies has recently been shown to offer many possibilities for the design of metamaterials [40–42].

A particularly striking example of friction amplifica-

tion in a multicontact assembly is provided by interleaved books [43–45], which exhibit extreme resistance to separation when pulled apart. A simple model based on the Amontons-Coulomb laws revealed that this exceptional strength arises from the action of the pulling operator: even a minimal frictional force acting at the boundaries, is nonlinearly amplified throughout the interior of the stack [43, 44]. This seemingly peculiar effect is, in fact, a generic feature that has been observed in a number of interleaved systems such as rolled ribbons [46], fiber-reinforced granular materials [47], mushroom-shaped [48] or chain-granular [49] interlocking assemblies and twisted yarns [50]. Remarkably, interleaved books have also inspired the design of tactile displays [51], switchable clutches [52] and triboelectric power generators [53].

Although stick-slip motion has revealed interesting features when granular materials, textiles and elastic slab stacks yield [12, 19, 36, 43, 54], a systematic study of stick-slip dynamics in assemblies subjected to friction amplification is lacking. This article focuses on interleaved paper blocks as a model system to explore how stick-slip dynamics emerge in assemblies with multiple self-amplified frictional contacts. We point out that paper has proven to be a particularly reliable material for foundational studies on stick-slip [55]. Moreover, earlier investigations into static friction and steady sliding in interleaved books, alongside the development of an analytical model that quantitatively matches experimental results [43–45], provide a solid foundation to extend the analysis to more complex dynamical behaviors like stick-slip.

The paper is organized as follows. In Sec. II, we describe the experimental setup and protocol. Sec. III discusses the stick-slip features manifested in the force-displacement curves obtained through traction tests. Here, our results are interpreted with the aid of the mechanical model for friction amplification proposed in Ref. [43] and a standard stick-slip model based on a spring-block system. In Sec. IV, we present an analysis that combines imaging and force measurements in order to understand the behavior of the global effective stiffness of the assembly. Finally, in Sec. V, we summarize our results and provide an outlook for future studies.

II. EXPERIMENTAL SETUP

Our samples consist of couples of Post-It® blocks (3M) carefully interleaved sheet by sheet on the non-glued sides. We cut the received squared blocks in the direction perpendicular to the glue layer, so that each one has a length of $L_t = 75$ mm, width $W = 45$ mm and contains $2M = 50$ sheets $\epsilon = 0.1$ mm thick. In our notation, we refer to single sheets on one side of the system with the index $n \in \{1, M\}$ that runs from the center of the assembly to the outer part. Using a press, two holes were punched in the top of the blocks so that they could be screwed into the connectors of a traction ma-

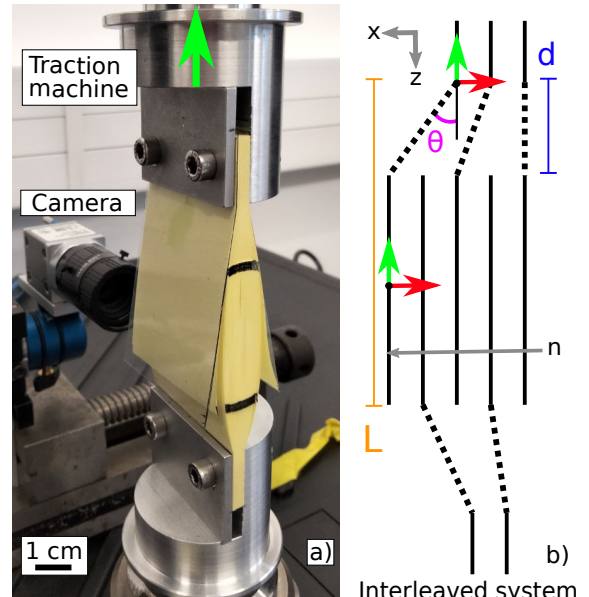


FIG. 1. a) Picture of the experimental setup. Two interleaved Post-it® blocks are mounted on a traction machine able to pull them apart by imposing a vertical displacement. A camera is placed behind the assembly to capture images of the interleaved zone during traction tests. The black marks on the block highlight the top and the bottom interleaving points. b) Schematic representation of the left-hand side of the interleaved assembly. A x - z reference system is defined. The sheets go from the clumping point to the interleaved point, forming an angle $\theta(n)$ that increases from the central to the external part of the assembly. According to these angles, the traction force (green arrows) is converted into orthogonal components (red arrows), which then compress the interleaved part of the assembly horizontally. The separation distance between the clumping and the interleaved point is denoted as d , while L is the distance between the clamping point and the end of a sheet.

chine (MTS Criterion Model 43) equipped with a force sensor with a load capacity of 1000 N (see Fig. 1a). Before clamping the system, we added an outer 0.3 mm thick plastic sheet (polyethylene terephthalate) on each external side of the upper block. These sheets help to create a more reproducible configuration of the outer part of the assembly and prevent sample deterioration during repeated manipulation. To ensure greater reproducibility of the experiments, the screws were tightened using a dynamometric screwdriver with a maximum torque of 1.2 Nm. Indeed, the amount of stress imposed at the clumping point influences the way the assembly deforms horizontally. Our experiments involved imposing a vertical detachment at a constant velocity V on the assembly, while measuring the total traction force F . The distance between the clamping point and the end of a sheet is considered constant and denoted as $L = 57$ mm. As can be seen more clearly in Fig. 7a, this distance does actually vary between external and internal sheets (i.e., external sheets are more bent). However, we neglected this vari-

ation in our schematization, as it corresponds to only 0.75% of L . To quantify the degree of entanglement of two blocks, we define the variable d , which corresponds to the separation distance from the clamping point to the interleaving point (see Fig. 1b). Upon the separation of the assembly, d increases along with the total distance between the upper and lower clumping points $L+d$. Meanwhile, the interleaved length $L-d$ decreases. The traction machine allows controlling the position of the upper clamp to micrometric precision with a 50 nm resolution. In order to image the system during the detachment, a high resolution camera (Basler a2A1920 - 160umPRO, 1920×1200 pixels²) equipped with a lens (Fujinon 12 mm 1:1.8) is placed along the direction parallel to the sheet width (see Fig. 1a). Once the assembly is secured in the traction machine, our experimental protocol consists of the following steps. First, we interleave the two blocks until we reach $d = d_0 - \delta d$, where $d_0 = 13$ mm and $\delta d = 35 \mu\text{m}$. During this process, the system deforms asymmetrically because the sheets do not always slide on each other in the same way on the left and right hand side of the assembly. We then gently tap the two blocks laterally to ensure that all the sheets fully slide on each other, making the system appear symmetric with respect to the vertical axis. Then, we set $d = d_0$. The system is now under tensile stress, so we gently tap again to make it relax. The force sensor is then set to zero and the measurement is started, with a vertical detachment imposed at the desired velocity V . This protocol ensures that different experiments start with a similar amount of residual stress in the assembly. The acquisition rate of our measurements is adjusted according to V in order to reliably resolve single stick-slip events during system detachment.

During preliminary experiments, we noted a marked aging effect: for a given sample, we need to repeat the traction test up to seven times before obtaining comparable $F(d)$ curves over consecutive runs. This is probably due to the aging of the contact asperities between the sheet surfaces. In the following, unless explicitly stated, we will always discuss results for which the effect of aging is negligible.

III. STICK-SLIP DYNAMICS

A. Force-displacement curve

Our main dataset consists of traction tests in a detachment range of $d \in [13, 18]$ mm, for four values of $V = \{0.5, 1, 5, 10\}$ mm/min. Here we start by discussing the main features of a typical force-displacement curve $F(d)$ obtained for a given velocity (see Fig. 2). The traction force initially increases, exhibiting a linear behavior (see bottom-left inset). After a few tens of micrometers, the system starts to exhibit stick-slip behavior, with an average increase in force until a maximum is reached. Through various experiments, we found that

the occurrence of stick-slip in the initial stage of the traction test, during which the system accumulates stress, depends on sample preparation. We interpret this regime as the system globally accumulating increasing stress, but with some local release due to residual heterogeneities in the initial configuration of the assembly. After the peak force, the system begins to detach progressively, still exhibiting stick-slip events, albeit with decreasing force on average. Resolving individual stick-slip events reveals that, contrary to the response observed in other complex frictional assemblies [36], the overall stick-slip motion appears strikingly regular after a few events exhibiting fluctuating amplitudes. The two upper-right panels of Fig. 2 show a zoom-in of single stick-slip events at early and later stages of detachment. Here we observe an evolution of the stick-slip features: in the first part of the detachment, the stick-slip amplitude is relatively large, and the force-displacement curve within a single event is asymmetric. In contrast, at larger d , the stick-slip amplitude is reduced, and the curve is more symmetric. By following the system dynamics with the camera (see Sec. IV A, and the Video in the Supplementary Material) we checked that, during the stick phase, the system deforms without changing its interleaved length $L-d$ (i.e. none of the sheets are sliding), while during the slip all the pages slide at the same time (within the resolution of our measurements) thus reducing $L-d$. In other words, as in standard frictional model (i.e. spring-block systems), the stress is accumulated upon system deformation and subsequently released by sliding.

B. Mechanical model for friction amplification

Contrary to standard scenarios where stick-slip dynamics is stationary in time, here, after each slip event, the system results to be less interleaved than before. As reported in previous studies, the frictional properties of the assembly are crucially dependent on how much the two blocks are entangled [43, 44]. In particular, a model was proposed to estimate the total frictional force \mathcal{T} that the system opposes to detachment:

$$\mathcal{T} = 2MT^* \sqrt{\frac{\pi}{4\alpha}} \exp(\alpha) \operatorname{erf}(\sqrt{\alpha}), \quad (1)$$

where $\alpha = 2\epsilon\mu M^2/d$, μ is the friction coefficient between the sheet surfaces and T^* is the friction force between the two outer pages on each side of the assembly. This model, which was validated against experimental data in Ref. [43], tells us that the total traction force results from the amplification of T^* (which is expected to be small) by a large factor that scales with the exponential of the square of the number of pages. In a subsequent study [44], it was clarified that the friction force T^* (typically of the order of mN) arises from the adhesion forces between the pages. We point out that Eq. (1) was derived based on the fact that the system's geometry allows for

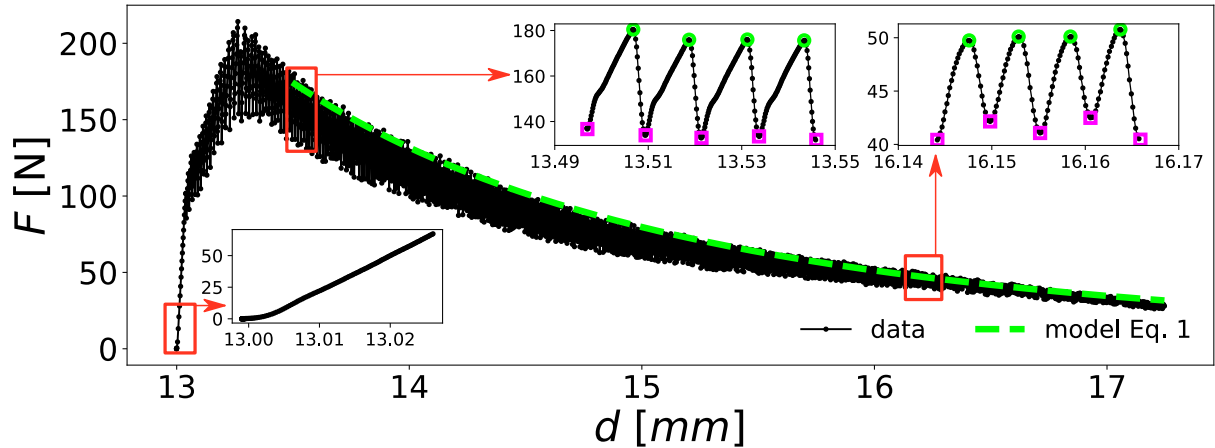


FIG. 2. Measured total traction force as a function of the separation distance for an experiment performed with pulling velocity $V = 10$ mm/min. From left to right, the insets show the system's initial elastic response, typical early-stage stick-slip events (high amplitude, asymmetric) and typical late-stage stick-slip events (low amplitude, symmetric). Green circles refer to local maxima F_{\max} within single stick-slip events (also defined as $F_p = F(d_p)$ in Sec. III C), pink squares refer to local minima defined as $F_v = F(d_v)$ in Sec. III C. The green dashed line in the main panel shows the result of fitting $F_{\max}(d)$ via Eq. (1) with $T^* = 3$ mN and $\mu = 0.89$.

a partial conversion of the vertical force applied by the traction machine into a horizontal component N acting on the interleaved part of the assembly (see the sketch in Fig. 1b). This conversion occurs for every sheet, each one feeling the contribution of all the outer sheets, resulting in an increasing local N going from outside to the internal part of the assembly. The model predicts a normal force felt by the sheet n due to the outer ones which reads:

$$N(n) = (T^*/2\mu)[\exp[\alpha(1 - (n/M)^2)] - 1]. \quad (2)$$

The above equation is obtained as a direct extension of the calculations performed in Ref. [43], which made use of the continuum limit $1/M \ll 1$. From Eq. (2), we can also estimate the average normal force felt by the assembly as a whole $\mathcal{N} = 4M \int_0^1 ds N(Ms) \sim \mathcal{T}/\mu$, where the integration variable $s = n/M$ is used to perform the continuum limit.

This model was originally used in studies that focused on verifying the predicted scaling with α , rather than on resolving the stick-slip dynamics, as in our case. The model does not consider the presence of stick-slip, however, Eq. 1 predicts the force needed to overcome the total static friction (considering all the sheets in static contact) given a certain geometric configuration of the assembly (which is parametrized by d). Within standard stick-slip models [27], the external traction force is equal to static friction at the start of the slip. This suggests using Eq. 1 to describe the evolution of the peak forces F_{\max} of stick-slip events as a function of d . In Fig. 2, we show the good agreement between Eq. (1) and the measured $F_{\max}(d)$. This agreement is obtained by using $\mu = 0.89$ and $T^* = 3$ mN, which is of the same order as the one obtained in Ref. [44]. Provided a rescaling with

the sheet width, our T^* is also compatible with the estimate based on paper-on-paper work of adhesion provided in the same reference. On the other hand, the fitted value of μ cannot be simply traced back to a single representative paper-on-paper static friction coefficient. Indeed, as already noted in previous studies [43, 56], adhesion forces introduce a divergence of the static friction coefficient for low normal forces between two surfaces (corresponding to a plateau of the friction force at zero normal force). Since we expect a non-negligible variation in the normal force between external and internal sheets according to Eq. (2), we decided to quantify the relevance of this effect for our system. In Appendix A, we show the measured paper-on-paper static friction coefficient for a couple of sheets in contact under a normal load varied between 0.1 and 2 N obtaining static friction coefficients between 1.2 and 0.54. The friction coefficient $\mu = 0.89$ obtained by fitting $F_{\max}(d)$ via Eq. 1 falls within the range of these values. Furthermore, it is close to the one obtained in Ref. [43] from experiments involving interleaved blocks of different dimensions and numbers of pages. The good agreement between experimental data and Eq. (1) shown in Fig. 2 demonstrates that the evolution of the maximum force achieved in a single stick-slip event can be explained by static properties alone, without considering the system's deformation.

C. Analysis of stick-slip features

We now focus on features of stick-slip events that, contrary to F_{\max} , cannot be directly interpreted based on the model developed in Ref. [43].

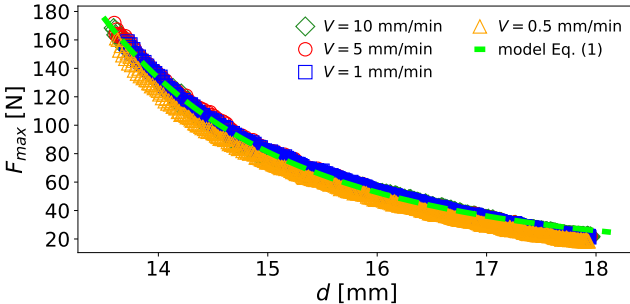


FIG. 3. Maximum local force within single stick-slip events as a function of the separation distance for different pulling velocities. The dashed line shows the prediction of Eq. (1) obtained with $T^* = 3$ mN and $\mu = 0.89$. The effects of velocity are negligible for this observable.

1. Stick-slip in a simple spring-block model

Before analyzing the experimental data, it is useful to recall the phenomenology of the simplest possible model exhibiting stick-slip motion namely a block of mass m under a normal load w and dragged through a spring of stiffness k on a surface characterized by a static friction coefficient μ_s and a dynamic one $\mu_d < \mu_s$. The free end of the spring is assumed to move at a fixed velocity v in the direction tangential to the surface. The elongation $u(t)$ of the spring with respect to its repose length is the only degree of freedom of the system, which also defines the elastic force $f(t) = ku(t)$ transmitted by the spring. This model exhibits stationary periodic stick-slip motion [27]: in the stick phase, the block is completely at rest and $f(t)$ increases linearly with time until reaching $f(t) = f_{\max} = \mu_s w$; then, the block slips moving under the combined effect of dynamic coulomb friction $\text{sign}(v)\mu_d w$ and elastic force until it stops. This marks the start of the next stick phase. In the low velocity limit $v \ll (\mu_s - \mu_d)w/\sqrt{mk}$, we have a simple analytical prediction for all the relevant stick-slip features, namely the stick time $t_{\text{st}} = 2(\mu_s - \mu_d)w/kv$, the slip time $t_{\text{sl}} = \pi\sqrt{m/k} \ll t_{\text{st}}$ and the spring elongation at the end of the slip $u_0 = (2\mu_d - \mu_s)w/k$. From these quantities we can easily obtain also the force amplitude of stick-slip events $\Delta f = \mu_s w - ku_0 = 2(\mu_s - \mu_d)w$. Already from these simple considerations, it is clear that three key control parameters to characterize stick-slip motion are k , w and v . They are also relevant for more elaborate mechanical models of stick-slip, including, for example, a rate- and state-dependent friction coefficient [25, 57]. For this reason, spring stiffness, normal load and pulling velocity are the main quantities that are varied in standard spring-block experimental settings [10, 55].

2. Force-displacement curves within stick-slip events

The only control parameter that can be mapped directly from a simple spring-block configuration to our system is the traction velocity V , which acts as v in the spring-block model. The effective stiffness of the interleaved assembly and the normal forces acting perpendicular to the sliding surfaces are both expected to depend non-trivially on the degree of entanglement of the two blocks (here quantified by d). We therefore begin by comparing stick-slip features for different values of V and d . First, we note that $F_{\max}(d)$ does not substantially depend on V for all the explored range of d (Fig. 3). A slight downward shift can be seen in the $V = 0.5$ mm/min curve, but this can be attributed to aging, given that this curve corresponds to the last experiment performed in chronological order. Nevertheless, we are able to fit all the obtained $F_{\max}(d)$ via Eq. (1), using the same $T^* = 3$ mN and $\mu = 0.890 \pm 0.005$. This is consistent with the scenario predicted by the spring-block model, where f_{\max} is independent of v regardless of whether the low velocity limit is satisfied. We specify here that, throughout our study, every time we fit $F_{\max}(d)$ via Eq. (1), we must add an offset T_0 to the latter, as our force signals are relative to $d = d_0$ (where the force sensor is set to zero). Across all our datasets, we obtained $T_0 \in [-10, 10]$ N, which is a small interval compared to the full range of values found in a typical $F_{\max}(d)$ curve.

We will now turn our attention to the force-displacement curve within individual stick-slip events. These events are identified by detecting local minima and maxima in $F(d)$. Each event begins at a local minimum $d = d_v$ and ends at the next local minimum, with the local maximum at $d = d_p$ occurring in between. It is also useful to define the local minimum force as $F_v = F(d_v)$ and the local maximum force as $F_p = F(d_p)$, which coincides with F_{\max} considered above (see also the two upper-right panels of Fig. 2). In Fig. 4, We plot $F - F_v$ as a function of $d - d_v$ for different d_v (in each panel) and V (in different panels). The stick-slip amplitude $\Delta F = F_p - F_v$, the stick length $\Lambda_{\text{st}} = d_p - d_v$ and the slip length Λ_{sl} are represented in Fig. 4d. For the remainder of the paper, the stick-slip features defined here will be labelled as a function of d_v . From Fig. 4, we observe that increasing d_v at fixed V , or vice versa, has the same qualitative effect of reducing ΔF and increasing $\Lambda_{\text{sl}}/\Lambda_{\text{st}}$ making the force-displacement curves appear more symmetrical. Nevertheless, the presence of a well-defined low velocity limit is indicated by the lack of significant change between the two lowest velocities, $V = 0.5$ and $V = 1$ mm/min. For these two cases, we note that the slips are almost instantaneous (i.e. $\Lambda_{\text{sl}}/\Lambda_{\text{st}} \sim 0$) and that the stick phase is characterized by a linear increase in force, which is well described by a single slope. In contrast, at $V = 5$ and $V = 10$ mm/min, the stick exhibits a steep slope at small displacements, followed by a gentler slope. We do not have a clear explanation for the presence of this double regime at high velocities; the observed phenomenology

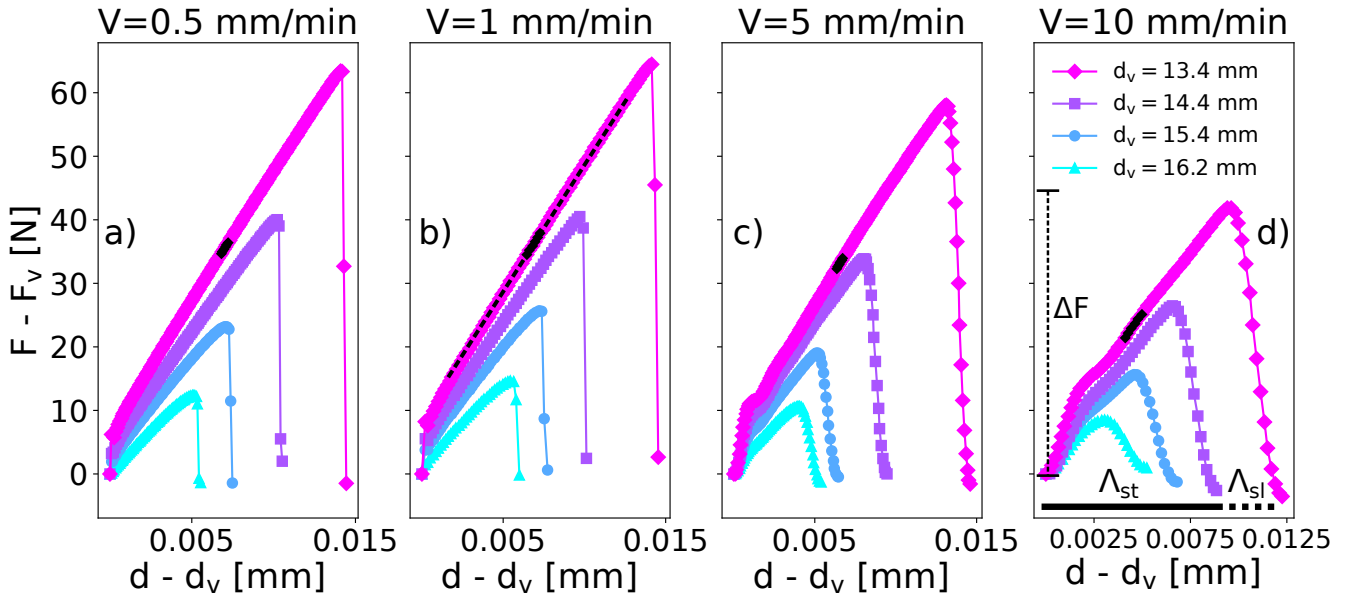


FIG. 4. Force-displacement curves within single stick-slip events. Different panels show data obtained at different pulling velocities. Within each panel, we show stick-slip events starting at different separation distances d_v , which correspond to local force minima. In panel d, we define the stick-slip amplitude ΔF as well as the stick Λ_{st} and slip Λ_{sl} lengths. Each panel shows (on the pink curve) the subset of points used to estimate the effective stiffness of the assembly from the slope of the central part of the stick phase. Panel b) explicitly illustrates that this slope is representative of a significant portion of the stick.

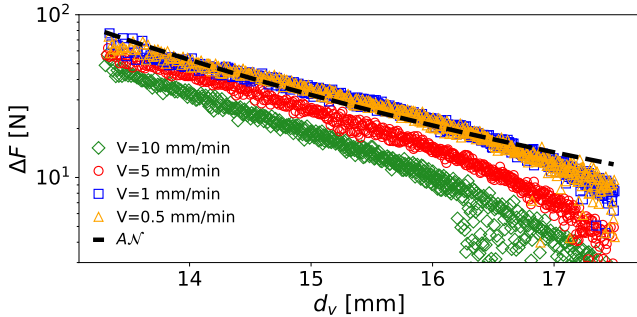


FIG. 5. Stick-slip amplitude as a function of the separation distance at the beginning of the stick for different pulling velocities. We note that the curves collapse at low velocities. The dashed line shows that the decay is relatively well approximated by the effective normal force acting on the assembly. This is proportional to the decay predicted by Eq. (1) with $T^* = 3$ mN and $\mu = 0.89$ through a prefactor A/μ , with $A = 0.34$.

suggests that it is a dynamical effect due to inertia. In what follows, we will mainly concentrate on the stick-slip features that survive in the low velocity regime.

3. Stick-slip amplitude

To make more quantitative considerations, we plot in Fig. 5 the stick-slip amplitude of all the detected events as a function of d_v for different velocities. Here we see

that the values of ΔF stabilize at low velocities, independently of d_v . We point out that an increase in stick-slip amplitude until saturation has been observed in experiments with sliding contact surfaces when the relative velocity decreases [58]. In order to elucidate this phenomenon, it was necessary to employ a realistic friction model that incorporated a sticking-time-dependent friction coefficient [26]. We also note that the curve at $V = 10$ mm/min changes from exhibiting relatively small fluctuations to large ones around $d_v \sim 16.2$. We checked that this corresponds to the occurrence of less regular stick-slip events, which could be linked to a transition from stick-slip to steady sliding [55] occurring in the outer region of the assembly, where normal force is low (see Eq. (2)).

Putting aside the these dynamical effects arising at large V , we now focus on the two $\Delta F(d_v)$ curves in the low velocity regime with the aim of understanding their decrease during the detachment. As discussed under Eq. (2), we expect the effective normal force \mathcal{N} felt by the assembly to decrease proportionally to \mathcal{T} . As shown in Fig. 5, combining Eq. (1) and (2), we verified that the range of values covered by our experimental data is compatible with $\Delta F(d_v) = A\mathcal{N}(d_v)$ with $A = 0.34$. Following the analogy with the spring-block model, where the stick-slip amplitude decreases proportionally to the normal load with a prefactor $2(\mu_s - \mu_d)$, we can interpret A as playing the role of this prefactor. As a further support of this interpretation, we point out that the estimated $A/2$ is very close to the value of $\mu_s - \mu_d$ obtained from our paper-on-paper friction characterization

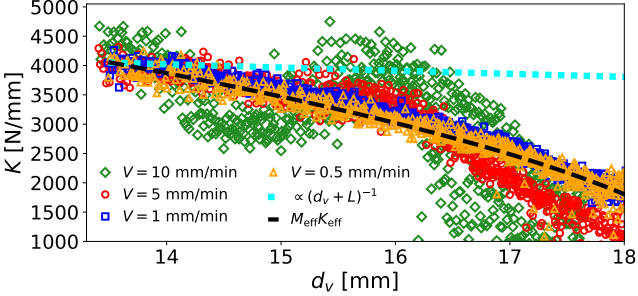


FIG. 6. Effective stiffness of the assembly as a function of the separation distance for different pulling velocities. This is estimated from the slope of the central part of the stick phase (see Fig. 4). Also for this observable, the curves collapse at low velocities. The cyan dotted curve provides a comparison with the stiffness decay expected from the increase in assembly length during the detachment. The black dashed curve shows our prediction based on the effective number of pages contributing to the global stiffness (see Sec. IV B). Data for $V = 5$ and 10 mm/min reflect the presence of a double regime in the force-displacement curves during the stick.

in the range of normal forces between 0.5 and 1 N, where $\mu_s \sim 0.61$ and $\mu_d \sim 0.44$ (see Appendix A). We also note, however, that the proportionality between $\Delta F(d_v)$ and $\mathcal{N}(d_v)$ is not in perfect agreement with the data. To better capture the functional form of this decay, it is probably necessary to improve the model proposed in Ref. [43] by taking into account stick-slip motion between contact surfaces. This is indeed a promising direction for future theoretical studies. From our analysis of Fig. 5, we can nevertheless conclude that the decrease of the stick-slip amplitude as a function of d_v is a consequence of the decrease in the effective normal force experienced by the contact surfaces in the assembly as it becomes less interleaved. The reduction in stick-slip amplitude with normal force can then be easily understood based on an analogy with the spring-block model.

4. Effective stiffness

We now analyze the behavior of the slope of the force-displacement curve during the stick phase. In particular, we focus on the low velocity limit, where we expect this slope to represent the effective stiffness of the assembly. By performing a linear fit of the central part of the force-displacement curve, we are sure to avoid possible non-linear effects due to the transition between stick and slip. This is, of course, only true for velocities where the stick phase is well described by a single linear regime. In Fig. 6, we show the effective stiffness K extracted from the central part of the force-displacement curve as a function of d_v for different velocities. As expected, we observe that the data exhibit the same behavior for $V < 5$ mm/min, indicating a well-defined low velocity limit with no significant dynamic effects during the stick phase. Focusing

on this limit, we observe that K monotonically decreases by a factor ~ 4 from the start to the end of the detachment. In other words, the assembly becomes softer as the degree of entanglement between the two blocks decreases. In order to better understand this behavior, we can first compare the measured values with the typical stiffness of the elementary elements of the assembly. Through traction tests performed on single paper sheets (see Appendix A), we estimate a Young's modulus of the paper $Y_p \in [2, 3]$ GPa. The stiffness of a single sheet under tensile stress would then be $K_p = \epsilon W Y_p / L \sim 200$ N/mm. Linking this elementary stiffness to that of the interleaved assembly is, however, not an easy task. By approximating the contribution of a couple of sheets with a series of two springs of stiffness K_p and then considering the whole assembly as the equivalent of $2M$ of these springs in parallel, one can estimate the global stiffness to be $2M(K_p/2) \sim 5000$ N/mm, which matches the order of magnitude of the measured values. However, this approach lacks a consistent way to predict the observed decrease of K as a function of d_v . By modelling the contribution of the individual sheets to the global stiffness more realistically, one could explain the decay of $K(d_v)$, considering that the assembly softens as its total length $L + d_v$ increases. In Fig. 6, we show that the expected stiffness decay $\propto (L + d_v)^{-1}$ appears almost flat in the explored range of d_v . In order to correctly understand the behavior of the global stiffness, it then becomes important to make more direct empirical observations of how the assembly deforms during detachment. This will be the main focus of the next section.

IV. THE ROLE OF DEFORMATION

A. Horizontal deformation by image processing

To take a closer look at how the system deforms during the detachment, we performed some experiments during which we acquired high resolution images of the assembly from the frontal view (see Fig. 7a). By looking at the videos obtained from these images (see Supplementary Materials), we observed the following key facts: i) within the time resolution of our videos, slip events occur at the same time for all the sheets, ii) during both the stick and slip phases, the sheets move in the direction perpendicular to the traction force, iii) this horizontal motion is more significant for the outer sheets than the inner ones. These observations are summarized in Figs. 7b-c where we show the space-time diagram during four stick-slip events for an external sheet ($n = 23$, panel d) and a more internal one ($n = 10$, panel c). These diagrams show the instantaneous pixel intensity averaged over a vertical interval of 0.84 mm in the upper part of the images (see the white mark in Fig. 7a). The horizontal axis represents the space interval around a sheet, the vertical axis represents the time evolution. It is clear that both sheets move inwards during the stick phase, until they experience an

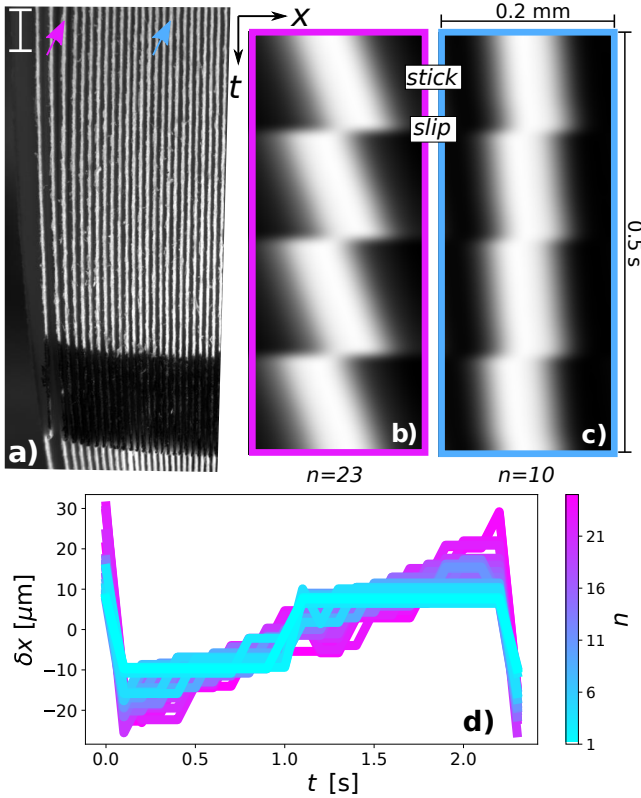


FIG. 7. a) Image of a portion of the interleaved part of the assembly. The black-colored region highlights the bottom interleaved point. The white mark in the upper part of the image refers to the 0.84 mm vertical interval over which pixel intensity is averaged to perform image processing. The colored arrows refer to the sheets used to produce the space-time diagram of panels b and c. Note that the external sheets are slightly bent outwards, whereas the internal ones are straight. b) Typical space-time diagram for an external sheet. It shows the time evolution of the pixel intensity in a 0.2 mm width horizontal interval centered around the $n = 23$ sheet. The considered time interval is 0.5 seconds and corresponds to the occurrence of four stick-slip events. c) Same as panel b but for an internal sheet ($n = 10$). It displaces significantly less than the outer sheet. d) Horizontal displacement between two slip events for all the sheets in the left-hand side of the assembly as a function of time. Outer sheets displace more than inner sheets. The data come from an event starting at $d = 13.4$ mm in a traction test at $V = 1$ mm/min .

almost instantaneous outward jump in correspondence with the slip. This indicates that during the stick phase, when the assembly accumulates tensile stress, it responds with horizontal compression; while it decompresses as the tensile stress is released in the slip. We also note that, during both the inward and outward motions, the external sheet moves across a wider horizontal interval than the internal one. As for the synchronicity of slip events, we believe it is true only at the timescale of our observation. An analogy with depinning models [59], suggests a possible scenario where a single sheet reaches the thresh-

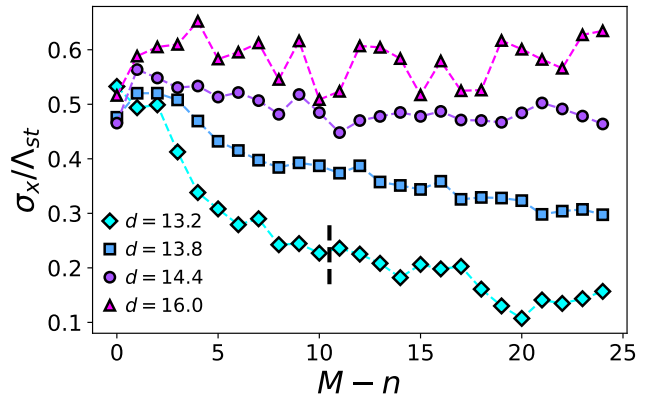


FIG. 8. Mean absolute horizontal displacement during stick phases normalized by the slip length as a function of the page index. The data come from a traction test at $V = 1$ mm/min. Each curve shows quantities averaged over 20 stick phases starting at separation distances in the range $d \in [13.2, 16]$ mm. At low, d outer sheets clearly displace more than the inner one. For less interleaved conditions, also the inner sheets displace significantly and the curves gradually assume a constant trend at higher values. The dashed vertical line indicate the typical M_{eff} estimated for at the beginning of the detachment (see Sec. IV B).

old of static friction and then starts to slip. This alters the mechanical balance of the other sheets, triggering an avalanche of slip events. Whether the avalanche initiation occurs randomly within the assembly or in a specific weak region that can be predicted using a detailed model of the interleaved assembly is an interesting question for future studies that could be answered by imaging the system with a high-speed camera.

We now focus on a detailed analysis of the horizontal system's deformation. From our images, we are able to detect the instantaneous horizontal position $x(n, t)$ of the n -th sheet in a given portion of the assembly (see Appendix B). As we did for the space-time diagrams, we will consider the horizontal position of the sheets in the upper part of the images. Based on the symmetry of the system, we focused on the left-hand side of the assembly. Denoting as t_v the starting time of the stick phases and with t_{st} their duration (which are both independent of n), we analyzed the horizontal displacement $\delta x(n, t_v + t) = x(n, t_v + t) - \hat{x}(n)$, where $\hat{x}(n) = 1/t_{st} \int_0^{t_{st}} x(n, t_v + t) dt$ is the average horizontal position of the sheet within the stick. In Fig. 7d, we plot δx as a function of $t \in [0, t_{st}]$ for $n \in [1, M]$ during a single stick-slip event. We note that this quantity captures the observation that the outer sheets tend to displace more than the internal ones. To measure the horizontal deformation of the system during the stick phases, we consider the mean absolute horizontal displacement $\sigma_x(n, t_v) = \sqrt{1/t_{st} \int_0^{t_{st}} \delta x^2(n, t_v + t) dt}$. As shown in Fig. 8, normalizing $\sigma_x(n, t_v)$ with the corresponding vertical stick length $\Lambda_{st}(t_v) = V t_{st}(t_v)$, allows us to analyze

the horizontal deformation of the assembly at different stages of detachment as a function of sheet index. For highly interleaved blocks, we obtain a quantitative description of the scenario suggested by Fig. 7d. Indeed, σ_x/Λ_{st} decreases as a function of $M-n$, meaning that the system's horizontal deformation reduces going from the external part to the internal part of the assembly. However, we also note that for less interleaved blocks, σ_x/Λ_{st} gradually assumes a constant trend, meaning that normal deformation becomes spatially homogeneous as the system detaches. This homogenization is accompanied by an increase in horizontal deformation across all the sheets. Focusing on the measured numerical values of σ_x/Λ_{st} , we also note that the external sheets undergoes horizontal displacements comparable to the vertical ones for the overall detachment. Instead, the inner part of the assembly initially experiences an almost negligible horizontal deformation before reaching the same relative deformation observed in the external part. At least in this regime (i.e. $d \sim 13.2$ mm), the assembly could be considered as consisting of an outer shell of highly mobile horizontal sheets and an inner shell in which the sheets respond to external traction with negligible horizontal displacement. This picture will be particularly relevant for the next section.

One way to qualitatively explain the observed behavior of the system's deformation perpendicular to the traction force is to consider how the force normal to the contact surfaces varies within the assembly. Even though the model developed in Ref. [43] does not take into account the deformability of the system, we can still use it to estimate the normal force $N(n)$ experienced by the sheets in the assembly using Eq. (2). As discussed in Sec. III B, we expect that the outer sheets experience a lower normal force, $N(n \sim M) \sim 0$, with respect to that felt by the inner ones $N(n \sim 1) \gg 1$. Combined with the behavior of σ_x/Λ_{st} discussed above, this reasonably suggests that the outer sheets, which experience a low N , are relatively more free to displace horizontally than the inner sheets, which experience a large N .

B. Effective number of sheets

Thanks to these insights into the system's horizontal deformation, we can now make an important step forward in understanding how the different sheets respond to the imposed *vertical* traction. First, we recall that for each sheet n in the assembly, we can define an angle $\theta(n, d) = \arctan(n\epsilon/d)$ between the vertical axis and the portion of the sheet connecting the clumping point to the start of the interleaved zone (see Fig. 1a). Each sheet under the static friction threshold can then respond to the imposed vertical displacement in two ways: by longitudinal elongation and/or by an inward horizontal displacement $\delta x(n, d) \leq d \tan(\theta) = n\epsilon$. While the maximum possible horizontal displacement is purely determined by the geometry, the actual one also depends on the normal

force $N(n, d)$ acting on the sheet. The more the sheet is horizontally compressed, the less it will be able to move. As a consequence, highly horizontally compressed sheets will mainly respond to imposed vertical motion through a longitudinal elongation of the order of the measured stick length Λ_{st} , thus with a stiffness $\propto \epsilon W Y_p / L$ where Y_p is the Young's modulus of the paper (see also the discussion in Sec. III C 4).

However, making an analogous estimate for less horizontally compressed sheets is not straightforward. From our images, we observed that they are slightly bent outwards (see again Fig. 7a). In this condition, despite the static friction constraint at the top interleaved point, these sheets can follow the imposed vertical motion without stretching by reducing their degree of bending (which involves local horizontal displacements).

As a crude approximation, we split the sheets in the assembly in two groups based on a horizontal compression threshold \hat{N} . Sheets identified by $n \leq M_{eff}$ such that $N(n, d) \geq \hat{N}$ are considered not free to move horizontally, thus responding to the vertical traction only through longitudinal stretching. The remaining less compressed sheets are instead considered as contributing with a negligible stiffness to the total effective one. Inverting Eq. (2), we can then obtain the following analytical expression for the number of sheets effectively contributing to the stiffness of the interleaved system:

$$M_{eff}(d) = M \sqrt{1 - \ln(1 + 2\mu\hat{N}/T^*)/\alpha}, \quad (3)$$

which depends on d through α . We can now come back to the problem of estimating the effective stiffness K of the whole assembly introduced in Sec. III C 4. Based on the above discussion, we consider K as the result of $2M_{eff}$ couples of sheets acting as springs with stiffness $K_{eff}/2 = \epsilon W Y_{eff}/(2L)$ in parallel, thus having $K(d) = M_{eff}(d)K_{eff}$. Here, Y_{eff} represents an effective Young modulus of the paper that we expect to be higher than the actual measured one Y_p as it compensates for our crude approximation that considers the less compressed $M - M_{eff}$ sheets contributing with a zero stiffness to K . As shown in Fig. 6, using Y_{eff} and \hat{N} as fitting parameters, we obtain a good agreement between the measured $K(d_v)$ and the function $M_{eff}(d_v)K_{eff}$ with $Y_{eff} = 3.8$ GPa and $\hat{N} = 0.57$ N. The fitted value of Y_{eff} is then reasonable as it is close but slightly larger than the measured Y_p . Regarding the fitted value of \hat{N} , in Appendix C, we discuss how we can link it with a typical confining normal force needed to bend a single sheet in the interleaved part of the assembly.

As a further test for the predictive power of our estimate of K , we now consider an additional series of experiments performed at $V = 0.5$ or 1 mm/mm (i.e. in the low velocity limit) with samples differently aged. The mechanical properties of assemblies are impacted by various aging effects. On the one hand, we expect aging to occur at the level of the surface-contact asperities. On the other hand, repeated traction protocols and sample manipulation can induce plastic deformation of the

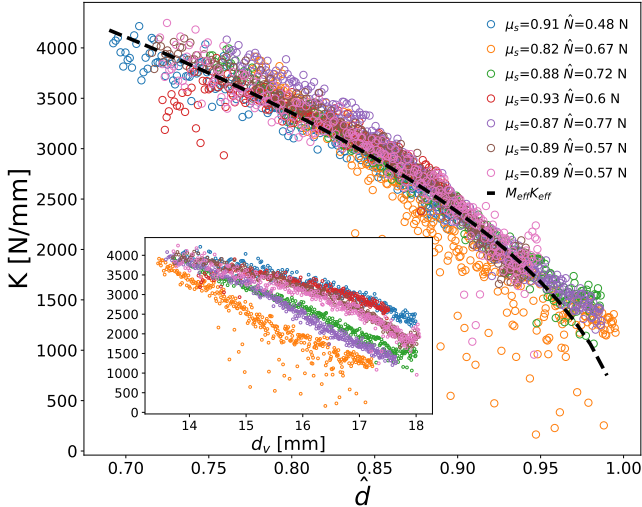


FIG. 9. Effective stiffness of the assembly as a function of the adimensionalized separation distance \hat{d} (defined in the text) for a series of traction test at $V = 1$ and $V = 0.5$ mm/min. Data are obtained from samples differently aged, thus presenting a certain variability. This is shown in the inset, where the same data are plotted as a function of the separation distance at the beginning of the stick. Using $Y_{\text{eff}} = 3.8$ GPa, $T^* = 3$ mN, different μ fitted from the $F(d)$ curves and adjusting \hat{N} , we are able to collapse all the data on the master curve predicted by our estimate based on the effective number of pages contributing to the global stiffness.

sheets, thereby altering their elastic response. This results in an observed variation of the force-displacement curves $F(d)$ and effective stiffness $K(d_v)$. Remarkably, for all the considered experiments, $F_{\text{max}}(d)$ can be fitted via Eq. 1 with the same $T^* = 3$ mN as the one used before and slightly varying the friction coefficient in the range $\mu \in [0.88, 0.93]$ (not shown). Keeping fixed these parameters along with $Y_{\text{eff}} = 3.8$ GPa, we fitted the curves $K(d_v)$ with via $M_{\text{eff}}(d)K_{\text{eff}}$ with only \hat{N} as a free parameter. In Fig. 9, we show that this procedure allows us to collapse all the data in a plot as a function of the adimensional variable $\hat{d} = \ln(1 + 2\mu\hat{N}/T^*)/\alpha$. As shown in the inset, the same data appear quite dispersed when plotted as a function of d_v .

We could now wonder about the possibility to establish a quantitative relation between the estimated M_{eff} and the system horizontal deformation measured through image processing. Looking again at the curves shown in Fig. 8, we do see that this is possible in the highly interleaved regime ($d = 13.2$) where the normalized mean absolute horizontal displacement exhibits a clear decay as a function of $n - M$. Considering the typical $M_{\text{eff}} = M\sqrt{1 - \hat{d}} \sim 11.3$ that we can estimate at the beginning of the detachment from our experiments, where $\hat{d} \sim 0.7$, we see that it corresponds to the region where $\sigma_x/\Lambda_{\text{st}}$ stabilizes at low values (cyan curve in Fig. 8). However, for less interleaved conditions, it is

not possible to identify two qualitatively different regions of the assembly based on the horizontal displacement of the sheets. The crude approximation of considering an effective number of sheets is then only quantitatively verified at low d , but is still able to capture the behavior of K throughout the entire detachment. This is probably because our modeling approach inherently incorporates the key mechanism for which sheets feeling less horizontal compression contribute less to the system's overall stiffness.

The agreement between the experimental data and our analytical estimate based on an effective number of sheets contributing to the global stiffness of the assembly, suggests that, when examining the mechanical response of interleaved systems (manifesting here as stick-slip motion), the subtle interplay between frictional and elastic properties and internal stress distribution must be considered. In continuum mechanics, the response to body deformation is usually predicted by considering only the material's elastic constants. However, complex mechanical assemblies, such as the one considered here, also require an understanding of how the distribution of internal stresses depends on the frictional contact properties between the interleaved objects. Our analysis is built on the idea that the effective number of sheets contributing to the stiffness of the assembly (Eq. (3)) is determined by the distribution of normal forces within it (Eq. 2), which in turn depend on paper-on-paper friction. The system's response is entirely due to the coupling between traction and compression made possible by a finite friction coefficient between the sheets, a frictionless assembly would not exhibit any resistance to traction. This is consistent with the limit predicted by Eq. (3) for which $M_{\text{eff}} \rightarrow 0$ when $\mu \rightarrow 0$. Taking all these ingredients into account, it is reasonable to find that, in the presence of such an emergent friction-driven cohesion, body deformation is governed by an effective stiffness that also depends on frictional properties.

V. CONCLUSION AND OUTLOOK

In this paper, we studied stick-slip motion in a system formed from two interleaved blocks of paper sheets. This system exhibits unusual friction amplification against block separation due to the conversion of traction force into compression, which increases friction between the contact surfaces within the assembly. Our force measurements enable us to resolve individual stick-slip events and study different dynamic features as a function of the imposed detachment velocity and the assembly's degree of entanglement. The stick-slip amplitude decreases as the system detaches and as the pulling velocity increases. We demonstrated that this behavior is linked to the overall normal compression experienced by the contact surfaces in the assembly and can be understood through an analogy with a simple frictional spring-block model. By combining force measurements with an imaging-based

analysis of the system's normal deformation, we analyzed the behavior of the assembly's global stiffness, estimated in the low velocity limit from the slope of the force-displacement curve in the stick phase. We found that this stiffness also decreases as the system detaches. This behavior can be explained by observing that the outer shell of the assembly deforms more than the inner shell in the horizontal direction during the stick phase. Consequently, the outer shell contributes less to the overall effective stiffness measured under vertical traction. We then analytically estimated the effective number of sheets contributing to the global stiffness, taking into account the variation in horizontal confinement due to normal forces in the assembly. The good agreement between the stiffness obtained through this estimation and the experimental data highlights the non-trivial interplay between the internal stress distribution and the mechanical properties of the system. Indeed, the number of sheets that effectively contribute to the stiffness of the assembly depends on how normal forces are distributed within it, which in turn depends on the friction between paper surfaces.

To the best of our knowledge, this is the first systematic study of stick-slip motion in a complex mechanical assembly involving multiple surfaces in contact and friction amplification properties. Interleaved books represent a model system for this type of assemblies, meaning that the analysis reported here is also relevant to granular, textile and fibrous materials, as well as metamaterials that exploit friction amplification mechanisms.

We will now conclude the paper by outlining potential future developments of this study.

Stick-slip instability analysis. When dealing with friction dynamics, a classic analysis concerns the transition between stick-slip and steady sliding. Empirical observations generally show that steady sliding becomes unstable with respect to stick-slip at high velocities, high normal forces, and low stiffness. Linear stability analyses of spring-block models with a rate and state-variable description, predict the instability of steady sliding when the ratio of spring stiffness to normal load is below a threshold that depends on the imposed velocity [55]. Extending this type of analysis to interleaved systems is

a valuable direction for future studies. However, suitable experimental protocols must first be designed, as the only control parameter that can be directly mapped into standard spring-block models is V . As demonstrated by the investigation in this paper, in an interleaved assembly experiencing the self-amplification of frictional forces, the effective normal load and stiffness relevant to stick-slip dynamics are complex emergent properties of the system.

Theoretical modeling. From a theoretical standpoint, we emphasize that, while the mechanical model proposed in Ref. [43] was useful for interpreting certain experimental results presented in this study, a more refined version of it that explicitly describes stick-slip motion would be a valuable tool for describing interleaved books and, more generally, for understanding the dynamics of systems with friction amplification. In this perspective, we identify three key aspects that would be considered in refining the model. First, a proper description of sheet elastic deformation combined with dynamic equations for paper-on-paper contact surfaces that are able to describe stick-slip motion. This could be achieved by modelling each couple of sheets as a spring-block system, possibly including a rate-and state-variable framework to perform local linear stability analysis. Second, one should consider the fact that the normal load increases during the stick phase. Indeed, as the traction force grows, so does its normal projection acting on the interleaved part. Third, it would be desirable also to properly include in the model the dependence of the static friction to the normal force due to adhesion (see also Appendix A).

Ultimately, we highlight the intriguing perspective of using high-speed imaging to analyze the spatiotemporal distribution of slip avalanches within the assembly.

ACKNOWLEDGMENTS

The authors acknowledge Sandrine Mariot for technical support in the use of the SoMaC&CoMic platform. This work has been funded by the Agence Nationale de la Recherche (ANR), France, grant ANR-21-CE06-0039.

[1] B. Bhushan, ed., *Fundamentals of tribology and bridging the gap between the macro- and micro/nanoscales*. NATO Science Series II, Dordrecht, Netherlands: Springer, Mar. 2001.

[2] A. Vanossi, N. Manini, M. Urbakh, S. Zapperi, and E. Tosatti, “Colloquium: Modeling friction: From nanoscale to mesoscale,” *Rev. Mod. Phys.*, vol. 85, pp. 529–552, 2013.

[3] H. M. Shewan, C. Pradal, and J. R. Stokes, “Tribology and its growing use toward the study of food oral processing and sensory perception,” *Journal of texture studies*, vol. 51, no. 1, pp. 7–22, 2020.

[4] I. M. Hutchings, “Leonardo da vinci's studies of friction,” *Wear*, vol. 360–361, pp. 51–66, 2016.

[5] Y. Desplanques, “Amontons-coulomb friction laws, a review of the original manuscript,” *SAE International Journal of Materials and Manufacturing*, vol. 8, no. 1, pp. 98–103, 2015.

[6] F. P. Bowden and D. Tabor, *The Friction and Lubrication of Solids*. Clarendon Press, 1950.

[7] T. Baumberger and C. Caroli, “Solid friction from stick-slip down to pinning and aging,” *Advances in Physics*,

vol. 55, no. 3-4, pp. 279–348, 2006.

[8] T. Baumberger and L. Gauthier, “Creeplike relaxation at the interface between rough solids under shear,” *Journal de Physique I*, vol. 6, no. 8, p. 1021–1030, 1996.

[9] C. H. Scholz, “Earthquakes and friction laws,” *Nature*, vol. 391, p. 37, 1998.

[10] T. Baumberger, P. Berthoud, and C. Caroli, “Physical analysis of the state- and rate-dependent friction law. ii. dynamic friction,” *Phys. Rev. B*, vol. 60, pp. 3928–3939, 1999.

[11] C. Marone, “Laboratory-derived friction laws and their application to seismic faulting,” *Ann. Revs. Earth & Plan. Sci.*, vol. 26, pp. 643–696, 1998.

[12] A. Baldassarri, F. Dalton, A. Petri, S. Zapperi, G. Pontuale, and L. Pietronero, “Brownian forces in sheared granular matter,” *Phys. Rev. Lett.*, vol. 96, p. 118002, Mar 2006.

[13] M. V. Rastei, B. Heinrich, and J. L. Gallani, “Puckering stick-slip friction induced by a sliding nanoscale contact,” *Phys. Rev. Lett.*, vol. 111, p. 084301, Aug 2013.

[14] M.-J. Dalbe, P.-P. Cortet, M. Cicotti, L. Vanel, and S. Santucci, “Multiscale stick-slip dynamics of adhesive tape peeling,” *Physical review letters*, vol. 115, no. 12, p. 128301, 2015.

[15] M. Marchand, F. Restagno, E. Rio, and F. Boulogne, “Roughness-induced friction on liquid foams,” *Phys. Rev. Lett.*, vol. 124, p. 118003, 2020.

[16] G. Petrillo, E. Lippiello, F. P. Landes, and A. Rosso, “The influence of the brittle-ductile transition zone on aftershock and foreshock occurrence,” *Nature Communications*, vol. 11, no. 1, p. 3010, 2020.

[17] A. Plati and A. Puglisi, “Collective drifts in vibrated granular packings: The interplay of friction and structure,” *Phys. Rev. Lett.*, vol. 128, p. 208001, 2022.

[18] C. Yan, H.-Y. Chen, P.-Y. Lai, and P. Tong, “Statistical laws of stick-slip friction at mesoscale,” *Nature Communications*, vol. 14, no. 1, p. 6221, 2023.

[19] W. Hu, Y. Ge, Q. Xu, R. Huang, Q. Zhao, H. Gou, M. McSaveney, C. Chang, Y. Li, X. Jia, and Y. Wang, “High time-resolved studies of stick-slip show similar dilatancy to fast and slow earthquakes,” *Proc. Natl. Acad. Sci. U. S. A.*, vol. 120, p. e2305134120, Nov. 2023.

[20] Y. Lu, D. Han, Q. Fu, X. Lu, Y. Zhang, Z. Wei, and Y. Chen, “Experimental investigation of stick-slip behaviors in dry sliding friction,” *Tribology International*, vol. 201, p. 110221, 2025.

[21] C. Dong, L. Shi, L. Li, X. Bai, C. Yuan, and Y. Tian, “Stick-slip behaviours of water lubrication polymer materials under low speed conditions,” *Tribology International*, vol. 106, pp. 55–61, 2017.

[22] Q. Zhang, J. Mo, Z. Xiang, Q. Liu, B. Tang, W. Jin, and S. Zhu, “The influence of interfacial wear characteristics on stick-slip vibration,” *Tribology International*, vol. 185, p. 108535, 2023.

[23] B. Armstrong-Helouvry, “Stick slip and control in low-speed motion,” *IEEE Transactions on Automatic Control*, vol. 38, no. 10, pp. 1483–1496, 2002.

[24] A. Plati, A. Petri, and M. Baldovin, “Control of friction: Shortcuts and optimization for the rate-and state-variable equation,” *European Journal of Mechanics A/Solids*, vol. 111, p. 105550, 2025.

[25] J. R. Rice and A. L. Ruina, “Stability of steady frictional slipping,” *J. Appl. Mech.*, vol. 50, pp. 343–349, 1983.

[26] C. Gao, D. Kuhlmann-Wilsdorf, and D. D. Makel, “The dynamic analysis of stick-slip motion,” *Wear*, vol. 173, no. 1-2, pp. 1–12, 1994.

[27] F.-J. Elmer, “Nonlinear dynamics of dry friction,” *Journal of Physics A: Mathematical and General*, vol. 30, no. 17, p. 6057, 1997.

[28] J. H. Jung, N. Pan, and T. J. Kang, “Generalized capstan problem: Bending rigidity, nonlinear friction, and extensibility effect,” *Tribology International*, vol. 41, no. 6, pp. 524–534, 2008.

[29] S. Ghosal, “Capstan friction model for dna ejection from bacteriophages,” *Physical review letters*, vol. 109, no. 24, p. 248105, 2012.

[30] W.-R. Su, C.-H. Chu, C.-L. Lin, C.-J. Lin, I.-M. Jou, and C.-W. Chang, “The modified finger-trap suture technique: a biomechanical comparison of a novel suture technique for graft fixation,” *Arthroscopy: The Journal of Arthroscopic & Related Surgery*, vol. 28, no. 5, pp. 702–710, 2012.

[31] J. W. Brown, E. Bullitt, S. Sriswasdi, S. Harper, D. W. Speicher, and C. J. McKnight, “The physiological molecular shape of spectrin: a compact supercoil resembling a chinese finger trap,” *PLoS computational biology*, vol. 11, no. 6, p. e1004302, 2015.

[32] C. Leech, “The modelling of friction in polymer fibre ropes,” *International Journal of Mechanical Sciences*, vol. 44, no. 3, pp. 621–643, 2002.

[33] O. Allan, T. Mishra, and M. d. Rooij, “Experimental analysis of contact forces between strands in three-strand ropes with varying twist parameters and filament counts,” *Text. Res. J.*, May 2025.

[34] O. Allan, T. Mishra, R. J. Meijer, and M. d. Rooij, “Micro-CT analysis of geometrical distribution of filaments in double-twisted three-strand ropes: Comparison with analytical model,” *J. Ind. Text.*, vol. 55, Apr. 2025.

[35] S. Poincloux, M. Adda-Bedia, and F. Lechenault, “Geometry and elasticity of a knitted fabric,” *Physical Review X*, vol. 8, no. 2, p. 021075, 2018.

[36] S. Poincloux, M. Adda-Bedia, and F. Lechenault, “Crackling dynamics in the mechanical response of knitted fabrics,” *Physical review letters*, vol. 121, no. 5, p. 058002, 2018.

[37] P. Schwartz, *Structure and mechanics of textile fibre assemblies*. Woodhead publishing, 2019.

[38] J. Duran, E. Kolb, and L. Vanel, “Static friction and arch formation in granular materials,” *Phys. Rev. E*, vol. 58, pp. 805–812, Jul 1998.

[39] F. Restagno, L. Bocquet, and E. Charlaix, “Where does a cohesive granular heap break?,” *The European Physical Journal E*, vol. 14, p. 177–183, June 2004.

[40] S. V. Franklin, “Geometric cohesion in granular materials,” *Physics today*, vol. 65, no. 9, pp. 70–71, 2012.

[41] N. Weiner, Y. Bhosale, M. Gazzola, and H. King, “Mechanics of randomly packed filaments—the “bird nest” as meta-material,” *Journal of Applied Physics*, vol. 127, no. 5, 2020.

[42] L. Dreier, T. J. Jones, A. Plummer, A. Košmrlj, and P.-T. Brun, “Beaded metamaterials,” *Nature communications*, vol. 16, no. 1, p. 7899, 2025.

[43] H. Alarcón, T. Salez, C. Poulard, J.-F. Bloch, É. Raphaël, K. Dalnoki-Veress, and F. Restagno, “Self-amplification of solid friction in interleaved assemblies,” *Physical review letters*, vol. 116, no. 1, p. 015502, 2016.

[44] R. Taub, T. Salez, H. Alarcon, É. Raphaël, C. Poulard,

and F. Restagno, "Nonlinear amplification of adhesion forces in interleaved books," *The European Physical Journal E*, vol. 44, no. 5, p. 71, 2021.

[45] R. Taub, *Assemblages d'objets élancés: mécanique et effets de contact*. PhD thesis, Université Paris-Saclay, 2020.

[46] N. Vani, A. Ibarra, J. Bico, É. Reyssat, and B. Roman, "Asymmetric bending boundary layer: The λ -test," *Proceedings of the National Academy of Sciences*, vol. 122, no. 11, p. e2426748122, 2025.

[47] L. Wierzchalek, G. Gauthier, and B. Darbois Texier, "Vane rheology of a fiber-reinforced granular material," *Journal of Rheology*, vol. 69, no. 3, pp. 353–363, 2025.

[48] P. Jiang, J. Qi, Z. Shi, H. Yang, and Y. Li, "Emergent neural network-like mechanical response in interlocking materials." 2025.

[49] D. Dumont, M. Houze, P. Rambach, T. Salez, S. Patinet, and P. Damman, "Emergent strain stiffening in interlocked granular chains," *Physical review letters*, vol. 120, no. 8, p. 088001, 2018.

[50] A. Seguin and J. Crassous, "Twist-controlled force amplification and spinning tension transition in yarn," *Physical Review Letters*, vol. 128, no. 7, p. 078002, 2022.

[51] S. An, X. Li, Z. Guo, Y. Huang, Y. Zhang, and H. Jiang, "Energy-efficient dynamic 3d metasurfaces via spatiotemporal jamming interleaved assemblies for tactile interfaces," *Nature Communications*, vol. 15, no. 1, p. 7340, 2024.

[52] A. Luo and A. J. Hart, "A switchable flexible mechanical clutch based on self-amplified friction of interleaved layers," *Extreme Mechanics Letters*, vol. 71, p. 102197, 2024.

[53] H. Huang, Z. Zhao, K. Tao, J. Wu, B. Ji, W. Yuan, and H. Chang, "Intersecting book inspired high-power-density electret/triboelectric multilayered power generator with flexible interdigital electrodes," in *2021 21st International Conference on Solid-State Sensors, Actuators and Microsystems (Transducers)*, IEEE, June 2021.

[54] S. Poincloux, P. M. Reis, and T. W. de Geus, "Stick-slip in a stack: How slip dissonance reveals aging," *Physical Review Research*, vol. 6, no. 1, p. 013080, 2024.

[55] F. Heslot, T. Baumberger, B. Perrin, B. Caroli, and C. Caroli, "Creep, stick-slip, and dry-friction dynamics: Experiments and a heuristic model," *Phys. Rev. E*, vol. 49, pp. 4973–4988, 1994.

[56] J. Crassous, L. Bocquet, S. Ciliberto, and C. Laroche, "Humidity effect on static aging of dry friction," *Europhysics Letters*, vol. 47, no. 5, p. 562, 1999.

[57] C. Gao, D. Kuhlmann-Wilsdorf, and D. D. Makel, "Fundamentals of stick-slip," *Wear*, vol. 162, pp. 1139–1149, 1993.

[58] S. Kato, K. Yamaguchi, T. Matsubayashi, and N. Sato, "Stick-slip motion and characteristics of friction in machine tool, slideway," *Memoirs of the Faculty of Engineering, Nagoya University*, vol. 27, no. 1, pp. 1–71, 1975.

[59] E. A. Jagla, F. P. Landes, and A. Rosso, "Viscoelastic effects in avalanche dynamics: A key to earthquake statistics," *Physical review letters*, vol. 112, no. 17, p. 174301, 2014.

[60] S. Achanta and J.-P. Celis, "On the scale dependence of coefficient of friction in unlubricated sliding contacts," *Wear*, vol. 269, no. 5-6, pp. 435–442, 2010.

[61] J. Gere and B. Goodno, *Mechanics of Materials, SI Edition*. Cengage Learning, 2008.

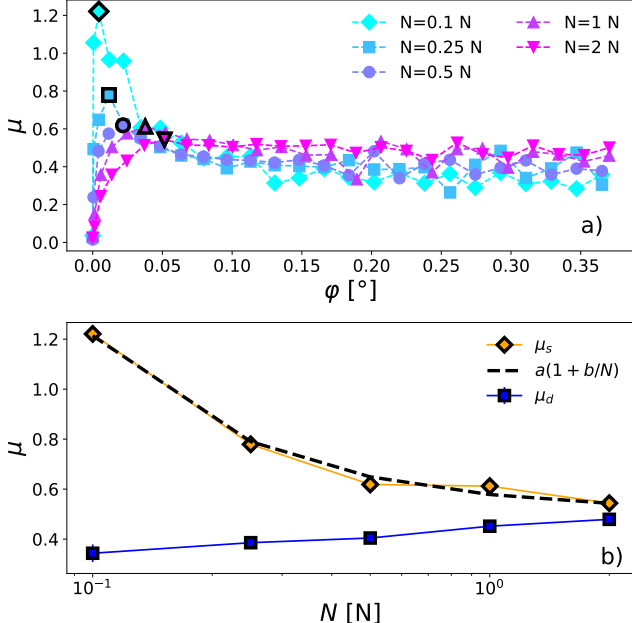


FIG. 10. a) Instantaneous friction coefficient as a function of the traveled angle for different imposed normal forces. The static friction coefficient is estimated from the local maxima of the curves, which are highlighted with black bordered markers. b) Static and dynamic friction coefficients as a function of the imposed normal force. The behavior of μ_s is well described by Eq. (A2). The dynamic friction coefficient has been obtained by averaging the curves $\mu(\varphi)$ over the range $\varphi \in [0.3, 120]^\circ$. Data have been obtained by making two Post-It paper surfaces slide on each other in a plane-plane geometry of a rheometer. These measurements have been performed with an imposed angular velocity $\Omega = 0.1$ rad/s.

Appendix A: Single sheets characterization

During our experimental investigation we characterized the mechanical properties of our Post-It® sheets.

Friction coefficients—First, we measured the paper-on-paper friction coefficients as a function of the normal force between two Post-It surfaces. This was done through a rheometer (Anton Paar, MCR 302) by covering the two sides of a plane-plane geometry with paper coming from the Post-It® sheets (adherence was assured by an adhesive tape). This geometry involves a circular contact area under a normal load N and a shear stress originated by the rheometer that imposes a rotation at angular velocity Ω . To convert the measured torque τ into a friction coefficient taking into account the shear imposed by relative rotation (and not by translation as in usual tribometers), we used the following formula

$$\mu = \frac{3}{2} \frac{\tau}{RN} \quad (\text{A1})$$

where $R = 25$ mm is the radius of the circular contact area. The above formula takes into account that the measured torque can be expressed as $\tau =$

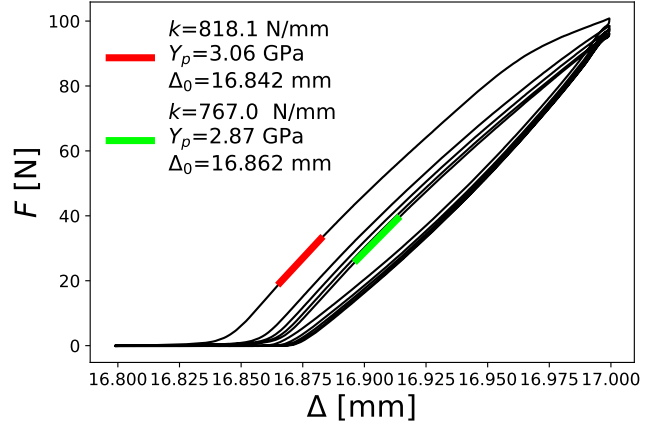


FIG. 11. Measured traction force as a function of the separation distance between the two clumping points for a single Post-It paper sheet. The vertical displacement is imposed at $V = 1$ mm/min and consists of 5 back-and-forth cycles. Different portions of the detachment branches can be fitted as $F = kd + F_0$. Then, one can take $Y_p = kd_0/\epsilon W$, where $d_0 = k/F_0$.

$\int_0^R dr \int_0^{2\pi} d\theta \mu N / (\pi R^2) r^2$, where the integrand represents the contribution of an infinitesimal contact area element at distance r from the center to the total torque. Our measurements were done starting at rest and recording the measured torque as a function of the traveled angle φ . From the resulting $\mu(\varphi)$ curves, we extract the static friction coefficient μ_s from the initial peak and the dynamic one μ_d averaging $\mu(\varphi)$ over the range $\varphi \in [0.3, 120]^\circ$ (see Fig. 10a). By repeating these measurements for different imposed normal forces $N \in [0.1, 2]$ N, we obtained $\mu_s(N)$ and $\mu_d(N)$ shown in Fig. 10b. We observe that μ_s decreases as a function of N while μ_d remains relatively constant showing only a slight increase over the whole range of N . The behavior of $\mu_s(N)$ can be explained based on the previous work by Crassous et al. [56] which, based on experimental evidences, proposed the following dependence of the static friction coefficient on the normal force:

$$\mu(N) = a(1 + b/N). \quad (\text{A2})$$

The divergence of the friction coefficient for vanishing normal mode is due to adhesion, which determines a non-zero friction force even when $N \rightarrow 0$. As shown in Fig. 10b, the measured paper-on-paper static friction coefficient shows a good agreement with Eq. (A2) having $a = 0.507$ and $b = 0.143$. As for explaining the slight increase of μ_d as a function of N , further investigations, which fall outside the scope of this paper, would be needed. Possible scenarios include a crossover between elastic and plastic contacts or the formation of wear particles [60].

Single sheet under tensile stress—We also estimated the Young's modulus of the paper by doing traction tests on single paper sheets. We imposed a vertical displace-

ment back and forth to a $\epsilon = 0.1$ mm thick, $L = 16.8$ mm long, and $W = 45$ mm wide sheet of Post-It® paper. In Fig. 11 we show an illustrative example of this analysis where the traction force F is plotted as a function of the distance Δ between the clumping points. The vertical displacement is imposed at $V = 1$ mm/min and consists of 5 back-and-forth cycles. The Young's modulus Y_p can be estimated by fitting different portions the detachment branches (i.e. the red and green lines in the figure) as $F = kd + F_0$. Then, one can take $Y_p = kd_0/\epsilon W$, where $d_0 = k/F_0$. By repeating this analysis for different sheets we obtained values of $Y_p \in [2, 3]$ Pa regardless of the imposed $V \leq 1$ mm/min.

Appendix B: Image processing

The analysis carried on in Sec. IV A is based on the detection of the instantaneous horizontal positions $x(n, t)$ of the sheets. These are extracted from the subregion of our frames corresponding to the white mark in Fig. 7a and shown in Fig. 12a. As depicted in Fig. 12b, we identify the horizontal position of the sheets by detecting the local maxima of the pixel intensity averaged over z in the aforementioned subregion. In Fig. 12c, we show that our method allows following the sheet horizontal displacement during stick-slip events.

Appendix C: Sheet bending

As discussed in Sec. IV B and sketched in Fig. 1b, the portion of the sheet joining the clumping point to the start of the interleaved part makes an angle $\theta(n)$ with the vertical axis. Without any additional confining force in the horizontal direction, a sheet would not adhere to the rest of the assembly, making an angle $\theta(n)$ with z not only at the clumping point but also at the interleaving point. This condition is indeed realized by the outer sheet in the assembly that has only the horizontal component of gravity as a confinement (see Fig. 1a). More internal sheets bend due to the normal force exerted by the outer sheets, thus resulting more parallel to the vertical axis. In order to estimate a typical bending force, we will consider sheets as cantilever beams with the upper end fixed at the interleaving point (see Fig. 13). Through beam mechanics [61] we obtain that to displace the application point of the force by a distance δ we need $\hat{N} = 3\delta I Y_p / \lambda^3$, where $I = \epsilon^3 W / 12$ is the second moment of inertia of the sheet and λ is the distance from the interleaving point and the application point of \hat{N} . Then, the displacement needed to make the sheet n adhere to the inner sheets of the assembly is $\delta = \lambda \tan \theta(n, d) = \lambda n \epsilon / d$. The application point λ of the normal force is not easy to estimate, we expect it to be not too distant from the interleaving point and having the interleaved length $L - d$ as an upper bound. Putting together the above expressions we can check that, taking outer sheets $n \in [15, 25]$, the in-

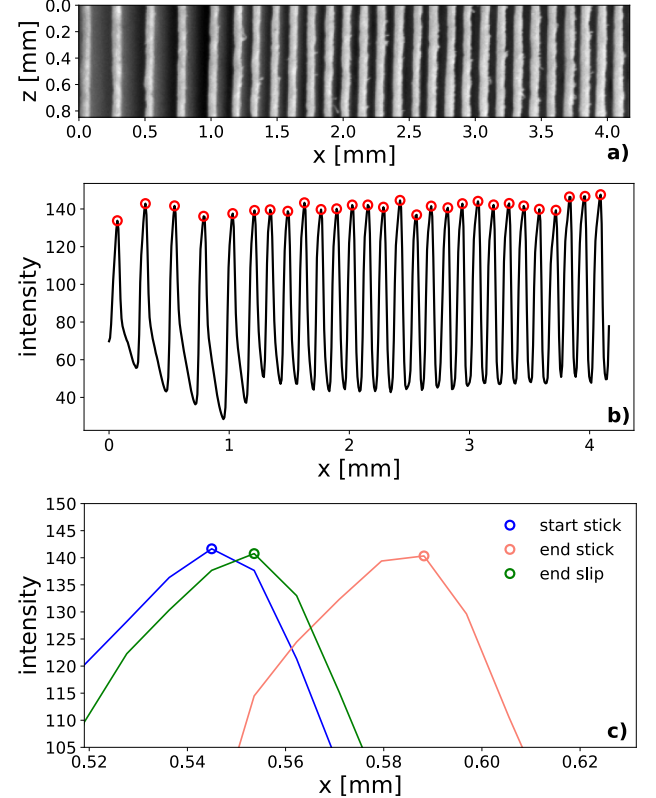


FIG. 12. a) Illustrative picture of the subregion of the images analyzed in Sec. IV A. b) Intensity averaged over z as a function of the horizontal pixel coordinate for one frame at the beginning of the stick phase. c) Zoom on pixel intensities in correspondence to an outer sheet for three frames: one at the beginning of the stick, one at the end of the stick, one at the end of the slip. The position clearly shifts inward during the stick and come back close to the initial one after the slip.

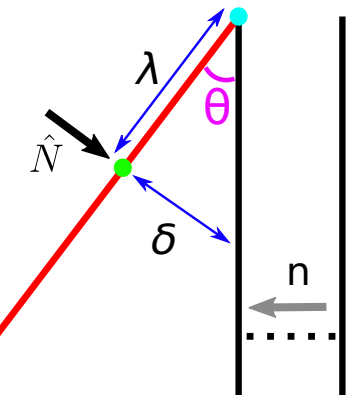


FIG. 13. An outer sheet (drawn in red) is schematized as a cantilever beam with the upper end fixed at the interleaving point (cyan circle). The application point of \hat{N} is represented by the green circle and is located at a distance λ from the interleaving point. We consider δ to be the typical distance that the force application point needs to displace in order for an outer sheet to adhere to the inner ones (drawn in black).

terleaving point within $d \in [13, 18]$ mm and the Young's modulus in the range $Y_p \in [2, 3.8]$ GPa, we find that to a fitted $\hat{N} = 0.57$ N corresponds a $\lambda = \sqrt{nWY_p\epsilon^4/4d\hat{N}} \in [1.8, 3.8]$ mm. If we consider the whole interval of fitted

values $\hat{N} \in [0.48, 0.77]$ N we obtain $\lambda \in [1.56, 4.14]$ mm. These correspond to reasonable ranges of values for λ , which tells us that the estimated threshold normal forces \hat{N} are compatible with the typical force needed to make a sheet adhere to the inner ones.